




**Experimental lower bounds to the classical capacity of quantum channels**Mario A. Ciampini <sup>1,2,\*</sup> Álvaro Cuevas <sup>3,2,†</sup> Paolo Mataloni<sup>2,‡</sup> Chiara Macchiavello<sup>4,5,§</sup> and Massimiliano F. Sacchi <sup>6,4,||</sup><sup>1</sup>*Vienna Center for Quantum Science and Technology (VCQ), Faculty of Physics, University of Vienna, Vienna A-1090, Austria*<sup>2</sup>*Quantum Optics Group, Dipartimento di Fisica, Università di Roma La Sapienza, Piazzale Aldo Moro 5, Roma I-00185, Italy*<sup>3</sup>*ICFO–Institut de Ciències Fotòniques, The Barcelona Institute of Science and Technology, Castelldefels (Barcelona) 08860, Spain*<sup>4</sup>*Dipartimento di Fisica, Università di Pavia, Via Agostino Bassi 6, Pavia I-27100, Italy*<sup>5</sup>*INFN-Sezione di Pavia, Via Agostino Bassi 6, Pavia I-27100, Italy*<sup>6</sup>*Consiglio Nazionale delle Ricerche - Istituto di Fotonica e Nanotecnologie (CNR-IFN), Piazza Leonardo da Vinci 32, Milano I-20133, Italy*

(Received 17 November 2020; accepted 7 June 2021; published 15 June 2021)

We show an experimental procedure to certify the classical capacity for noisy qubit channels. The method makes use of a fixed bipartite entangled state, where the system qubit is sent to the channel input and the set of local measurements,  $\sigma_x \otimes \sigma_x$ ,  $\sigma_y \otimes \sigma_y$ , and  $\sigma_z \otimes \sigma_z$ , is performed at the channel output and the ancilla qubit, thus without resorting to full quantum process tomography. The witness to the classical capacity is then achieved by reconstructing sets of conditional probabilities, noise deconvolution, and classical optimization of the pertaining mutual information. The performance of the method to provide lower bounds to the classical capacity is tested by a two-photon polarization entangled state in Pauli channels and amplitude damping channels. The measured lower bounds to the channels are in high agreement with the simulated data, which take into account both the experimental entanglement fidelity  $F = 0.979 \pm 0.011$  of the input state and the systematic experimental imperfections.

DOI: [10.1103/PhysRevA.103.062414](https://doi.org/10.1103/PhysRevA.103.062414)**I. INTRODUCTION**

The complete characterization of quantum channels by quantum process tomography [1–11] is demanding in terms of state preparation and/or measurement settings since for increasing dimension  $d$  of the system Hilbert space it scales as  $d^4$ . When one is interested in certifying specific properties of a quantum channel, more affordable procedures can be devised without resorting to complete quantum process tomography. This is the case of the detection of entanglement-breaking properties [12,13] or non-Markovianity [14] of quantum channels, or the certification of lower bounds to the quantum capacity of noisy quantum channels [15–18]. Typically, these direct methods also have the advantage of being more precise with respect to complete process tomography, which has the drawback of involving larger statistical errors due to error propagation.

One of the most relevant properties of quantum channels is the classical capacity [19–21] for its operational importance in the quantification of the classical information that can be reliably transmitted. For the purpose of detecting lower bounds to the classical capacity, an efficient and versatile procedure has been recently proposed in Ref. [22]. The method allows one

to experimentally detect lower bounds to the classical capacity of completely unknown quantum channels just by means of a few local measurements, even for high-dimensional systems [23].

The gist of the procedure is to efficiently reconstruct a number of probability transition matrices for suitable input states (playing the role of “encoding”) and matched output projective measurements (the corresponding “decoding”). The method is accompanied by the optimization of the prior distribution for the single-letter encoding pertaining to each input-output transition matrix. In this way, the mutual information for different communication settings is recovered and the resulting values are compared. Hence, a lower bound to the Holevo capacity and then a certification of the minimum reliable transmission capacity is achieved. Similarly to the method of certification for the quantum capacity [15–17], here each of the conditional probabilities corresponding to a communication setting can be obtained by preparing just an initial fixed bipartite state, where only one party enters the quantum channel, while local measurements are performed at the input and output of the channel.

In this paper, we present an experimental demonstration for the above certification of classical capacity in noisy qubit channels. We implement the method by using highly pure polarization entangled photons pairs, where the encoding and decoding settings are achieved by exploiting complementary observables of the polarization state. Moreover, a faithful deconvolution of noise is performed over the experimental data, which allows one to optimize the reconstruction of the probability transition matrices.

\* mario.arnolfo.ciampini@univie.ac.at

† Alvaro.Cuevas@icfo.eu

‡ paolo.mataloni@uniroma1.it

§ chiara@unipv.it

|| msacchi@unipv.it

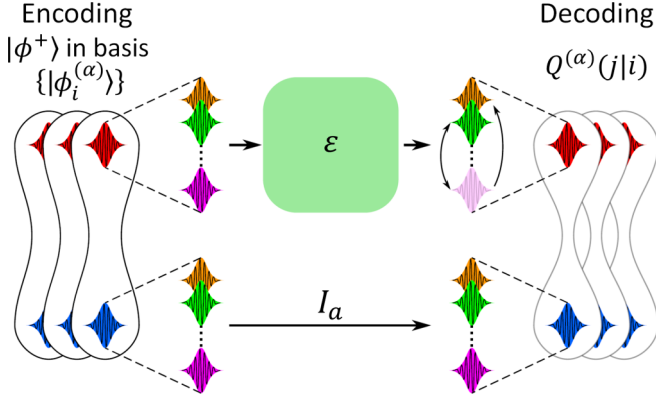


FIG. 1. Protocol concept. The  $s$  qudit of a maximally entangled bipartite quantum state  $|\phi^+\rangle$  is sent through a noisy quantum channel  $\mathcal{E}$ , while the  $a$  qudit propagates freely. Encoding-decoding of type  $\alpha$  is represented by layers and is achieved by locally measuring the basis  $\{|\phi_i^{(\alpha)}\rangle\}$ . The conditional probability  $Q^{(\alpha)}(j|i)$  of measuring  $|\phi_j^{(\alpha)}\rangle$  for an input  $|\phi_i^{(\alpha)}\rangle$  allows one to evaluate the Shannon capacity  $C^{(\alpha)}$ . The witness  $C_D$  of the classical capacity is the largest of the values  $\{C^{(\alpha)}\}$  among all tested types  $\alpha$ .

## II. THEORETICAL MODEL

Let us briefly review the method proposed in Ref. [22] for bounding from below the classical capacity, with specific attention to the case of single-qubit quantum channels.

The classical capacity  $C$  of a noisy quantum channel  $\mathcal{E}$  quantifies the maximum number of bits that can be reliably transmitted per channel use, and it is given by the regularized expression [19–21]  $C = \lim_{N \rightarrow \infty} \chi(\mathcal{E}^{\otimes N})/N$ , with  $N$  as the number of uses, in terms of the Holevo capacity,

$$\chi(\Phi) = \max_{\{p_i, \rho_i\}} \left\{ S \left[ \Phi \left( \sum_i p_i \rho_i \right) \right] - \sum_i p_i S[\Phi(\rho_i)] \right\}, \quad (1)$$

where  $S(\rho) = -\text{Tr}[\rho \log_2 \rho]$  denotes the von Neumann entropy. The Holevo capacity  $\chi(\mathcal{E}) \equiv C_1$ , also known as one-shot classical capacity, is a lower bound for the ultimate channel capacity  $C$ , and also an upper bound for the mutual information [24–26],

$$I(X; Y) = \sum_{x,y} p_x Q(y|x) \log_2 \frac{Q(y|x)}{\sum_{x'} p_{x'} Q(y|x')}, \quad (2)$$

where any transition matrix  $Q(y|x)$  corresponds to the conditional probability for outcome  $y$  in an arbitrary measurement at the output of a single use of the channel with input  $\rho_x$ , and  $p_x$  denotes an arbitrary prior probability, which corresponds to the distribution of the encoded alphabet on the quantum states  $\{\rho_x\}$ .

As depicted in Fig. 1, in order to obtain a witness for the classical capacity without resorting to complete process tomography, one can proceed as follows: Prepare a bipartite maximally entangled state  $|\phi^+\rangle = \frac{1}{\sqrt{d}} \sum_{k=0}^{d-1} |k_s\rangle |k_a\rangle$  between a system and ancillary spaces, both with dimension  $d$ ; send  $|\phi^+\rangle$  through the unknown channel by keeping the action of  $\mathcal{E}$  on the system alone, namely, via the map  $\mathcal{E} \otimes \mathbb{I}_a$ ; finally, locally measure a number of observables of the form  $X_\alpha \otimes X_\alpha^\tau$ , where  $\tau$  denotes the transposition with respect to the fixed basis defined by  $|\phi^+\rangle$ .

In fact, by denoting the  $d$  eigenvectors of  $X_\alpha$  as  $\{|\phi_i^{(\alpha)}\rangle\}$ , from the identity [27]

$$\text{Tr}[(A \otimes B^\tau)(\mathcal{E} \otimes \mathbb{I}_a)|\phi^+\rangle\langle\phi^+|] = \frac{1}{d} \text{Tr}[A\mathcal{E}(B)], \quad (3)$$

with arbitrary operators  $A$  and  $B$ , the detection scheme allows one to reconstruct the set of conditional probabilities,

$$Q^{(\alpha)}(j|i) = \langle\phi_j^{(\alpha)}| \mathcal{E}(|\phi_i^{(\alpha)}\rangle\langle\phi_i^{(\alpha)}|) |\phi_j^{(\alpha)}\rangle. \quad (4)$$

For each encoding-decoding scheme  $\alpha$  characterized by the choice of  $X_\alpha$ , we can write the corresponding optimal mutual information, namely, the Shannon capacity,

$$C^{(\alpha)} = \max_{\{p_i^{(\alpha)}\}} \sum_{i,j} p_i^{(\alpha)} Q^{(\alpha)}(j|i) \log_2 \frac{Q^{(\alpha)}(j|i)}{\sum_l p_l^{(\alpha)} Q^{(\alpha)}(j|l)}. \quad (5)$$

Then, we have the chain of inequalities,

$$C \geq C_1 \geq C_D \equiv \max_{\alpha} \{C^{(\alpha)}\}, \quad (6)$$

where  $C_D$  is the experimentally accessible witness that depends on the chosen set of measured observables labeled by  $\alpha$ , and provides a lower bound to the classical capacity of the unknown channel.

In the present scenario, we consider single-qubit channels, and the information settings correspond to the choice of the three local observables  $\sigma_x \otimes \sigma_x$ ,  $\sigma_y \otimes \sigma_y$ , and  $\sigma_z \otimes \sigma_z$ . Hence, each of the three conditional probabilities  $Q^{(\alpha)}(j|i)$ , with  $\alpha = x, y, z$ , is a  $2 \times 2$  transition matrix that corresponds to a binary classical channel, for which the optimal prior probability  $\{p_i^{(\alpha)}\}$  can be theoretically evaluated [22]. In fact, without loss of generality, for each transition matrix we can fix the labeling of logical zeros and ones such that  $0 \leq \epsilon_0 \leq \frac{1}{2}$ ,  $\epsilon_0 \leq \epsilon_1$ , and  $\epsilon_0 \leq 1 - \epsilon_1$ , where  $\epsilon_0$  denotes the error probability of receiving 1 for input 0, and  $\epsilon_1$  denotes the error probability of receiving 0 for input 1. Then, for each  $\alpha = x, y, z$ , the mutual information as in Eq. (5) is maximized by a prior probability  $\{p_0, p_1 = 1 - p_0\}$ , with

$$p_0 = \frac{1 - \epsilon_1(1 + z)}{(1 - \epsilon_0 - \epsilon_1)(1 + z)}, \quad (7)$$

where  $z = 2^{\frac{H[\epsilon_0] - H[\epsilon_1]}{1 - \epsilon_0 - \epsilon_1}}$ , and  $H(p) = -p \log_2 p - (1 - p) \log_2 (1 - p)$  denotes the binary Shannon entropy. The corresponding capacity is given by [22]

$$C_B(\epsilon_0, \epsilon_1) = \log_2 \left[ 1 + 2^{\frac{H[\epsilon_0] - H[\epsilon_1]}{1 - \epsilon_0 - \epsilon_1}} \right] + \frac{\epsilon_0}{1 - \epsilon_0 - \epsilon_1} H[\epsilon_1] - \frac{1 - \epsilon_1}{1 - \epsilon_0 - \epsilon_1} H[\epsilon_0]. \quad (8)$$

Notice that for  $\epsilon_0 = \epsilon_1 = \epsilon$ , one recovers the classical capacity for the binary symmetric channel,

$$C_B(\epsilon, \epsilon) = 1 - H[\epsilon], \quad (9)$$

with uniform optimal prior  $\{1/2, 1/2\}$ , whereas for  $\epsilon_0 = 0$  (i.e., when only input 1 is affected by error), one obtains the capacity of the so-called Z channel,

$$C_B(0, \epsilon) = \log_2 \left[ 1 + (1 - \epsilon)\epsilon^{\frac{\epsilon}{1-\epsilon}} \right]. \quad (10)$$

In Appendix A, we summarize the expected theoretical results for the qubit channels that we implemented experimentally.

In order to consider the experimental imperfections in our state preparation, we assume a Werner form,

$$\rho_F = \frac{4F - 1}{3} |\Phi^+\rangle \langle \Phi^+| + \frac{1 - F}{3} \mathbb{I}_s \otimes \mathbb{I}_a, \quad (11)$$

where  $F = \langle \Phi^+ | \rho_F | \Phi^+ \rangle$  denotes the fidelity with respect to the ideal maximally entangled state  $|\Phi^+\rangle = \frac{1}{\sqrt{2}}(|0\rangle|0\rangle + |1\rangle|1\rangle)$ . Hence, we can replace Eq. (3) with

$$\begin{aligned} \text{Tr}[A\mathcal{E}(B)] &= \frac{2}{4F - 1} \text{Tr}[(A \otimes \{3B^T - 2(1 - F) \\ &\quad \times \text{Tr}[B]\mathbb{I}_a\})(\mathcal{E} \otimes \mathbb{I}_a)\rho_F]. \end{aligned} \quad (12)$$

Equation (12) allows one to deconvolve the noise as long as  $F \neq 1/4$  since the output state  $(\mathcal{E} \otimes \mathbb{I}_a)\rho_F$  faithfully represents the unknown channel  $\mathcal{E}$ .

The normalized conditional probabilities for the three binary classical channels corresponding to the information settings  $\alpha = x, y, z$ , where coding and decoding are performed using the eigenstates of the three Pauli matrices  $\sigma_x, \sigma_y, \sigma_z$ , can be obtained by the ratio  $\frac{\text{Tr}[A\mathcal{E}(B)]}{\text{Tr}[\mathcal{E}(B)]}$ , when replacing  $A$  and  $B$  with the pertaining eigenvectors. In practical terms, these quantities are measured from the bipartite qubit detections, which in optical channels correspond to two-photon coincidence detections  $C(ji) = \text{Tr}[(|j\rangle\langle j|_S \otimes |i\rangle\langle i|_A)(\mathcal{E} \otimes \mathbb{I}_a)\rho_F]$  on the output state. We provide, in Appendix B, the explicit expressions for the conditional probabilities in terms of the measured coincidences. For each information setting  $\alpha = x, y, z$ , the logical bits and their pertaining transition error probabilities  $\epsilon_0^{(\alpha)}$  and  $\epsilon_1^{(\alpha)}$  introduced before Eq. (7) are identified from the conditional probabilities as follows:

$$\epsilon_0^{(\alpha)} = \min_{\{i,j\}} Q^{(\alpha)}(i|j) \equiv Q^{(\alpha)}(1|0), \quad \epsilon_1^{(\alpha)} \equiv Q^{(\alpha)}(0|1). \quad (13)$$

Using Eq. (8), from the experimental data we then obtain  $C^{(\alpha)} = C_B(\epsilon_0^{(\alpha)}, \epsilon_1^{(\alpha)})$ , and hence the detected classical capacity as

$$C_D = \max_{\alpha=x,y,z} C_B(\epsilon_0^{(\alpha)}, \epsilon_1^{(\alpha)}). \quad (14)$$

We remark that the effect of a fidelity value  $F < 1$  (except the case  $F = \frac{1}{4}$ ) is not detrimental for accessing the capacity witness  $C_D$ , and only the statistical noise is expected to increase for decreasing value of  $F$ . This can be argued from the identity (12) which, for any couple of bases  $\{|i\rangle_A\}_{i=0,1}$  and  $\{|j\rangle_S\}_{j=0,1}$ , provides an unbiased estimation of the joint probabilities  $p_F(j, i) = \text{Tr}[(|j\rangle\langle j|_S \otimes |i\rangle\langle i|_A)(\mathcal{E} \otimes \mathbb{I}_a)\rho_F]$  pertaining to the case of ideal fidelity  $F = 1$  in terms of the measured probabilities as

$$p_{F=1}(j, i) = \frac{1 + 2F}{4F - 1} p_F(j, i) - \frac{2(1 - F)}{4F - 1} p_F(j, i \oplus 1). \quad (15)$$

By denoting with  $\sigma$  the typical order of magnitude of the standard deviation for the measured joint probabilities with  $F < 1$ , the noise deconvolution provides the correct probabilities with standard deviation,

$$\begin{aligned} \sigma_F &= \sigma \sqrt{\left(\frac{1 + 2F}{4F - 1}\right)^2 + 4\left(\frac{1 - F}{4F - 1}\right)^2} \\ &= \sigma \frac{\sqrt{8F^2 - 4F + 5}}{|4F - 1|}. \end{aligned} \quad (16)$$

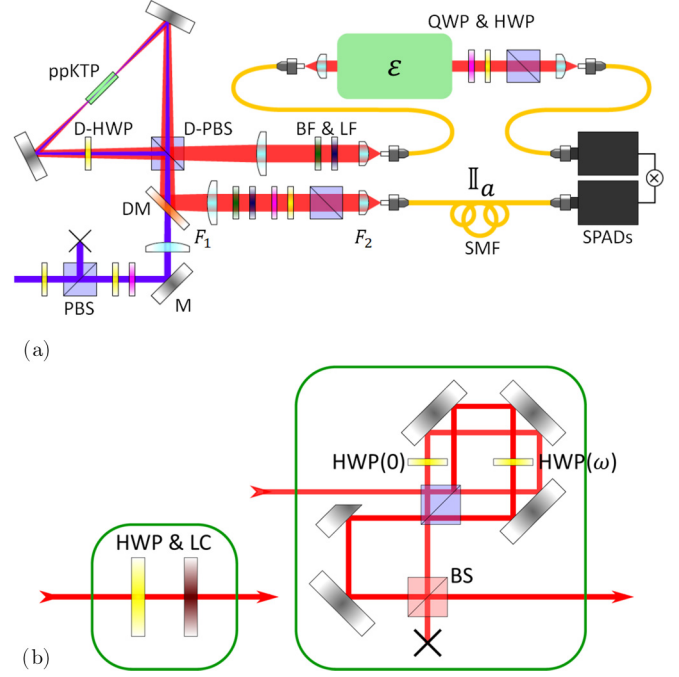


FIG. 2. (a) Full scheme with quantum source, propagation channels, and projection and measurement devices. PBS: polarizing beam splitter; M: mirror; BS: nonpolarizing 50:50 beam splitter; QWP: quarter-wave plate; HWP: half-wave plate; DM: dichroic mirror; ppKTP: periodically poled nonlinear crystal; BF: band-pass filter; LF: long-pass filter;  $F_k$ : lenses; SPADs: single-photon avalanche detectors; SMF: single-mode fiber; LC: liquid crystal element. The additional D-label is for compatibility with both the pump and generated wavelength. (b) Left: Setup for phase-damping and depolarizing channels. Right: Setup for amplitude damping channel.

### III. EXPERIMENTAL IMPLEMENTATION

A single-mode continuous-wave laser at 405 nm was used to pump a Type-II ppKTP crystal within a Sagnac interferometer (SI) in order to produce polarization-entangled photon pairs at 810 nm via spontaneous parametric down conversion, as implemented in [17]. The two output modes were labeled as  $s$  qubit and  $a$  qubit, so the Bell state  $|\Phi^+\rangle = \frac{1}{\sqrt{2}}(|H_s\rangle|H_a\rangle + |V_s\rangle|V_a\rangle)$  was generated. As shown in the full scheme of Fig. 2, tube lenses with  $F_1 = 300$  mm collimate both output modes, while objective lenses with  $F_2 = 11$  mm couple them into single-mode fibers (SMFs).

The fidelity of the experimental state  $\rho_F$  defined in Eq. (11) and measured by quantum tomography techniques [28,29] was  $F = \langle \Phi^+ | \rho_F | \Phi^+ \rangle = 0.979 \pm 0.011$ . Hence, we use Eq. (12) for noise deconvolution, and the standard deviation of the joint probabilities is increased just by 1.45% with respect to the ideal case  $F = 1$ , according to Eq. (16).

The observables  $\sigma_\alpha$ , for  $\alpha = x, y, z$ , are measured with rotations of a quarter-wave plate (QWP) and a half-wave plate (HWP) before a polarizing beam splitter (PBS) for each qubit. The remaining photon pairs after these projections are measured with synchronized single-photon avalanche detectors (SPADs) within a time window of 5 ns for an integration time of 10 s/measurement.

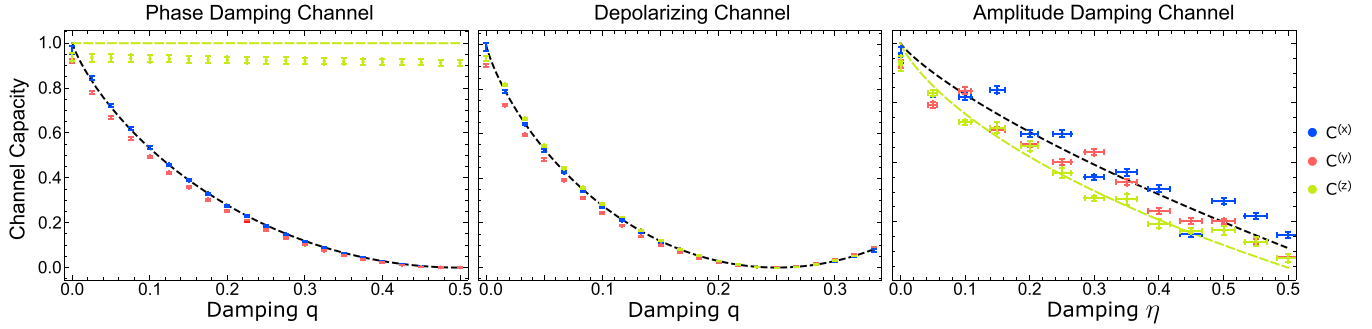


FIG. 3. Experimental channel capacity. Left:  $C^{(\alpha)}$  for PD channel. Center:  $C^{(\alpha)}$  for D channel. Right:  $C^{(\alpha)}$  for AD channel. In blue (dark gray):  $C^{(x)}$ ; in red (gray):  $C^{(y)}$ ; in green (light gray):  $C^{(z)}$ . For the predicted theoretical behavior,  $C^{(z)}$  is depicted with dashed green (light gray), while  $C^{(x)}$  and  $C^{(y)}$  are depicted with dashed black lines. All error bars (standard deviation) are calculated from at least eight values per point; their  $x$ -axis components originate from the propagated uncertainty in the angle of the HWPs, which dominate over other sources of error, such as wrong retardance in the LC.

By referring to the parametrization of channels given in Appendix A, within the family of Pauli channels we have chosen two special cases as implemented in [17,30]. The first one is the phase-damping (PD) channel (described by  $q_z = q$  and  $q_x = q_y = 0$  in Appendix A). The second one is the depolarizing (D) channel (described by  $q_x = q_y = q_z = q$ ). Their experimental simulations were implemented by  $q_i$ -weighted combinations of independent Pauli operations, achieved by setting a HWP at  $0^\circ$  degrees ( $45^\circ$  degrees) for  $\sigma_z$  ( $\sigma_x$ ) and a liquid crystal (LC) at minimum (maximum) voltage for  $\sigma_z$  (II) [see Fig. 2(b)]. Accordingly, the simultaneous operation  $\sigma_y = i\sigma_x\sigma_z$  gives us the last Pauli operation.

The experimental simulation of an amplitude damping (AD) channel was achieved by using a square SI with displaced trajectories as implemented in [17,31], where a HWP at  $0^\circ$  degrees was placed in the H-polarized counterclockwise trajectory, while another HWP at  $\omega = \frac{\arccos(-\sqrt{1-\eta})}{2}$  degrees was placed in the V-polarized clockwise trajectory. The induced rotation of a single polarization (or damping) sends this light to the long arm of an unbalanced Mach-Zehnder interferometer (MZI), which then recombines it out of coherence in a nonpolarizing beam splitter (BS).

#### IV. RESULTS

In Fig. 3, we show the measured Shannon capacities  $C^{(\alpha)}$  in all three bases for the experimental simulation of three different environments, namely, a PD channel, a D channel, and an AD channel. This is compared to the predicted behavior for the real input state, which is fidelity dependent from Eq. (12) and explained in detail in Appendix B. See Appendix C for details of the noise propagation and Appendix D for details of the experimental raw data.

For a PD channel, the witness  $C_D$  of the channel capacity is obtained for  $\alpha = z$  and can be compared with the expected theoretical value  $C_D = 1$ . The presented results confirm the behavior in which phase-damping processes do not affect binary data transmission in the logical basis, but only in complementary superposition bases. The systematic offset below unity value is due to the propagation of error by replacing experimental negative values of  $\epsilon_0^{(z)}$  with their absolute values. We observe that the customary constrained maximum-

likelihood technique can solve the possible issue of negative reconstructed probabilities and the resulting bias in the capacity bounds.

For a D channel, the theoretical value  $C_D = 1 - H(2q)$  is equally achieved by any of the three bases. Here, we find the best agreement with respect to this prediction because small differences of the experimental state or channel from the ideal ones are rapidly compensated during the decoherence process by the simultaneous action of all three Pauli operations. Accordingly, the balance increase (decrease) in the diagonal (off-diagonal) terms of the density matrix reduces bias projections and final data dispersion.

For an AD channel, the experimental implementation requires control on multiple optical paths, where systematic error can have an unbalanced contribution among different bases. Such an issue, combined with the nonlinear dependency of  $\eta$  with respect to  $\omega$  and an angular uncertainty of  $0.5^\circ$  degrees, gives considerable propagated errors. The expected capacity witness  $C_D = 1 - H(\frac{1-\sqrt{1-\eta}}{2})$  is equivalently achieved by the bases  $x$  or  $y$ . Our method still succeeds in showing the general behavior and providing a sensible lower bound to the classical channel capacity.

In summary, by comparison with the theoretical predictions, the method proved to be very effective in providing a witness for the classical capacity of noisy quantum channels, even if the channel implementation has critical and systematic imperfections. Moreover, by means of the noise deconvolution, we have shown that the method is robust with respect to an imperfect probe-state preparation and provides an unbiased estimation of the theoretical lower bounds.

#### V. CONCLUSIONS

The experimental coincidence counts allow one to directly reconstruct the sets of conditional probabilities for three different information settings. For each setting  $\alpha = x, y, z$ , by Eq. (13) the logical bits and the values of  $\epsilon_0^{(\alpha)}$  and  $\epsilon_1^{(\alpha)}$  are identified. From these values, one recovers three values of  $C_B$  as in Eq. (8), which correspond to the Shannon capacity, namely, the optimized mutual information for coding and decoding on the eigenstates of  $\sigma_x$ ,  $\sigma_y$ , and  $\sigma_z$ . The highest among such three values is selected as a classical capacity

witness, namely, it certifies a lower bound to the ultimate classical capacity of the unknown quantum channel. For each information setting, by Eq. (7) the identified values of  $\epsilon_0^{(\alpha)}$  and  $\epsilon_1^{(\alpha)}$  also allow one to obtain the optimal weight for the coding of the two logical characters.

We emphasize that our method is highly robust against experimental imperfections, even in cases where the prepared quantum state is partially mixed as the Werner state. For each of the three chosen bases, the Shannon capacity is precisely retrieved for all values of the channel parameters. Nevertheless, the most accurate values were obtained for the Pauli channels, which are effectively produced by mixing unitary operations over the input state. For mixtures of nonunitary operations as the amplitude damping channel, we find a less smooth behavior in the detected classical capacity because experimental imperfections do not act in balanced ways for both photon polarizations.

We recommend this method for certifying the classical capacity of quantum channels due to its high precision under different scenarios. The studied cases were not particularly designed to match with the protocol, but chosen to represent a variety of classes. No prior information is needed about the channel structure, while the measurement settings are much less demanding with respect to full process tomography.

#### ACKNOWLEDGMENTS

The work of Á.C. was supported by Becas Chile Grant No. 74200052 from the Chilean National Agency for Research and Development (ANID). C.M. acknowledges support by the European Quanterra Project QuICHE.

#### APPENDIX A: EXPECTED THEORETICAL RESULTS FOR THE IMPLEMENTED QUBIT CHANNELS

For an *amplitude damping (AD) channel*, described by

$$\mathcal{E}^{AD}(\rho) = K_0 \rho K_0^\dagger + K_1 \rho K_1^\dagger, \quad (\text{A1})$$

where  $K_0 = |0\rangle\langle 0| + \sqrt{1-\eta}|1\rangle\langle 1|$  and  $K_1 = \sqrt{\eta}|0\rangle\langle 1|$ , the

error probabilities of the three binary channels correspond to

$$\begin{aligned} \epsilon_0^{(x)} = \epsilon_1^{(x)} = \epsilon_0^{(y)} = \epsilon_1^{(y)} &= (1 - \sqrt{1-\eta})/2, \\ \epsilon_0^{(z)} = 0, \quad \epsilon_1^{(z)} &= \eta. \end{aligned} \quad (\text{A2})$$

The detected capacity is obtained equivalently by the  $x$  or  $y$  information setting and is given by

$$C_D = C^{(x)} = C^{(y)} = 1 - H\left(\frac{1 - \sqrt{1-\eta}}{2}\right). \quad (\text{A3})$$

For any  $\eta$ , this result outperforms the  $z$  setting, for which one has  $C^{(z)} = C_B(0, \eta)$ , according to Eq. (10). We recall that the detected capacity in Eq. (A3) is strictly lower than the Holevo capacity  $C_1$ , which can be evaluated as [32,33]

$$C_1 = \max_{t \in [0,1]} \{H[t(1-\eta)] - H[g(\eta, t)]\}, \quad (\text{A4})$$

where  $g(\eta, t) \equiv \frac{1}{2}[1 + \sqrt{1 - 4\eta(1-\eta)t^2}]$ .

For a *Pauli (P) channel*, described by

$$\mathcal{E}^P(\rho) = q_{\mathbb{I}}\rho + q_x\sigma_x\rho\sigma_x + q_y\sigma_y\rho\sigma_y + q_z\sigma_z\rho\sigma_z, \quad (\text{A5})$$

with  $q_{\mathbb{I}} = 1 - (q_x + q_y + q_z)$  and  $q_x + q_y + q_z \leq 1$  (with  $q_i \geq 0$ ), the three channels that are compared are symmetric and correspond to the error probabilities

$$\begin{aligned} \epsilon_0^{(x)} = \epsilon_1^{(x)} &= \min\{q_y + q_z, 1 - (q_y + q_z)\}, \\ \epsilon_0^{(y)} = \epsilon_1^{(y)} &= \min\{q_x + q_z, 1 - (q_x + q_z)\}, \\ \epsilon_0^{(z)} = \epsilon_1^{(z)} &= \min\{q_x + q_y, 1 - (q_x + q_y)\}. \end{aligned} \quad (\text{A6})$$

The detected capacity is then given by

$$C_D = 1 - \min\{H(q_y + q_z), H(q_x + p_z), H(q_x + p_y)\}, \quad (\text{A7})$$

where  $\min\{\cdot\}$  compares the  $x$ ,  $y$ , and  $z$  information settings, respectively. We recall that for Pauli channels, the capacity witness  $C_D$  equals the Holevo and the classical capacity (i.e.,  $C = C_1 = C_D$ ) since the additivity hypothesis holds true for unital qubit channels [34].

#### APPENDIX B: PROBABILITY TRANSITION MATRICES FOR THE THREE INFORMATION SETTINGS $\sigma_z, \sigma_x, \sigma_y$

From Eq. (12), the ratio  $\frac{\text{Tr}[A\mathcal{E}(B)]}{\text{Tr}[\mathcal{E}(B)]}$  is given by

$$\frac{\text{Tr}[A\mathcal{E}(B)]}{\text{Tr}[\mathcal{E}(B)]} = \frac{\text{Tr}[(A \otimes \{3B^T - 2(1-F)\text{Tr}[B]\mathbb{I}_a\})(\mathcal{E} \otimes \mathbb{I}_a)\rho_F]}{\text{Tr}[(\mathbb{I}_s \otimes \{3B^T - 2(1-F)\text{Tr}[B]\mathbb{I}_a\})(\mathcal{E} \otimes \mathbb{I}_a)\rho_F]}. \quad (\text{B1})$$

When qubits are encoded in the single-photon polarization degree of freedom, the  $z$ -information setting corresponds to the choice of  $A$  and  $B$  as the projectors on the basis  $\{|H\rangle, |V\rangle\}$ , with  $H$  ( $V$ ) as the horizontal (vertical) polarization. Using Eq. (B1), the corresponding probability transition matrix is then given in terms of the measured coincidences,  $C(ji) = \text{Tr}[(|j\rangle\langle j|_S \otimes |i\rangle\langle i|_A)(\mathcal{E} \otimes \mathbb{I}_a)\rho_F]$  as

$$Q^{(z)}(H|H) = \frac{(1+2F)C(HH) - 2(1-F)C(HV)}{(1+2F)[C(HH) + C(VH)] - 2(1-F)[C(HV) + C(VV)]}, \quad Q^{(z)}(V|H) = 1 - Q^{(z)}(H|H), \quad (\text{B2})$$

$$Q^{(z)}(H|V) = \frac{(1+2F)C(HV) - 2(1-F)C(HH)}{(1+2F)[C(HV) + C(VV)] - 2(1-F)[C(HH) + C(VH)]}, \quad Q^{(z)}(V|V) = 1 - Q^{(z)}(H|V). \quad (\text{B3})$$

For the  $x$ -information setting,  $A$  and  $B$  correspond to the projectors on the diagonal basis,  $|+\rangle = \frac{1}{\sqrt{2}}(|H\rangle + |V\rangle)$  and  $|-\rangle = \frac{1}{\sqrt{2}}(|H\rangle - |V\rangle)$ , and so one has

$$Q^{(x)}(+|+) = \frac{(1+2F)C(++ ) - 2(1-F)C(+-)}{(1+2F)[C(++ ) + C(-+)] - 2(1-F)[C(+-) + C(--)]}, \quad Q^{(x)}(-|+) = 1 - Q^{(x)}(+|+), \quad (\text{B4})$$

$$Q^{(x)}(+|-) = \frac{(1 + 2F)C(+-) - 2(1 - F)C(++)}{(1 + 2F)[C(+-) + C(--)] - 2(1 - F)[C(++) + C(-+)]}, \quad Q^{(x)}(-|-) = 1 - Q^{(x)}(+|-). \quad (\text{B5})$$

Finally, for the  $y$ -information setting,  $A$  and  $B$  correspond to the projectors on the circular basis,  $|R\rangle = \frac{1}{\sqrt{2}}(|H\rangle - i|V\rangle)$  and  $|L\rangle = \frac{1}{\sqrt{2}}(|H\rangle + i|V\rangle)$ , and hence

$$Q^{(y)}(R|R) = \frac{(1 + 2F)C(RL) - 2(1 - F)C(RR)}{(1 + 2F)[C(RL) + C(LL)] - 2(1 - F)[C(RR) + C(LR)]}, \quad Q^{(y)}(L|R) = 1 - Q^{(y)}(R|R), \quad (\text{B6})$$

$$Q^{(y)}(R|L) = \frac{(1 + 2F)C(RR) - 2(1 - F)C(RL)}{(1 + 2F)[C(RR) + C(LR)] - 2(1 - F)[C(RL) + C(LL)]}, \quad Q^{(y)}(L|L) = 1 - Q^{(y)}(R|L). \quad (\text{B7})$$

Notice the different symmetry in the equations for the  $y$  coding with respect to the  $z$  and  $x$  cases due to the presence of the transposition in Eq. (B1). For each of the above binary classical channels, the transition errors  $\epsilon_0^{(\alpha)}$  and  $\epsilon_1^{(\alpha)}$  are identified from the conditional probabilities by Eq. (13).

According to the above equations, all expectation values are obtained just by the measurement of 12 polarization projections of the state (4 by each of the 3 observables), which makes the process efficient in terms of the registration and analysis of the data, given the reduced number of operations compared with standard process tomography.

### APPENDIX C: DETECTION EFFICIENCIES AND EXPERIMENTAL ERROR ANALYSIS

The overall optical efficiencies for both system and ancilla modes are given by

$$\epsilon_s = \epsilon_{\text{Opt}} \cdot \epsilon_{\text{channel}} \cdot \epsilon_{\text{SMF}}^2 \cdot \epsilon_{\text{SPAD}}, \quad (\text{C1})$$

$$\epsilon_a = \epsilon_{\text{Opt}} \cdot \epsilon_{\text{SMF}} \cdot \epsilon_{\text{SPAD}}, \quad (\text{C2})$$

where the single-photon transmission efficiency of the main optical components is  $\epsilon_{\text{Opt}} = 0.9$ , the single-mode fiber coupling efficiency is  $\epsilon_{\text{SMF}} = 0.73$ , and the SPADs detection efficiency is  $\epsilon_{\text{SPAD}} = 0.7$ . Accordingly, the two-photon optical efficiency was

$$\epsilon_{s,a} = \epsilon_s \cdot \epsilon_a \approx 0.15 \cdot \epsilon_{\text{channel}}. \quad (\text{C3})$$

The channel optical efficiencies  $\epsilon_{\text{channel}}$  were 0.6 for the AD channel and 0.98 for the PD channel and D channel. Thus, the overall coincidence efficiencies  $\epsilon_{s,a}$  are 0.09 and 0.15, respectively.

The propagated standard deviation in our data was calculated from Monte Carlo simulations of Poissonian statistics on the photon coincidence counts. In our experiment, the main sources of error were the following:

- (1) The setting of the rotation angle in the LC and HWPs.
- (2) The setting of the LC voltage for the precise retardance.
- (3) The statistical propagation due to the mixing of independent Pauli operations.

The first source of error is negligible because all wave plates contained in the channels and used for the projective measurements and the LC were calibrated to a precision of  $\pm 0.1$  degrees. For wave plates at an angle around  $0^\circ$  degrees or  $45^\circ$  degrees, the dependence of counts on a small angle deviation is linear, and thus the overall error is strongly dominated by the Poissonian statistics on the counts. This is not valid in the AD-channel configuration, where the interference leads to a strong nonlinearity between wave-plate angles and coincidence counts, governed by  $\omega = \frac{\arccos(-\sqrt{1-\eta})}{2}$ . Accordingly, we considered a prudent error ( $0.5^\circ$  degrees) on the angle, leading to a considerable increase of the error on the damping parameter.

The second source of error is negligible as well because when performing the calibration of the LC, we use horizontally polarized light, the LC at 45 degrees, and a PBS. Here, by scanning the voltage on the LC, we verified a nonlinear retardance, which is almost flat around both the minimum and maximum voltages used in the experiment,  $V_{\text{low}} = 0.5$  V

TABLE I. Experimental conditional probabilities in the AD channel.

$\eta$	$Q^{(z)}(H H)$	$Q^{(z)}(V H)$	$Q^{(x)}(+ +)$	$Q^{(x)}(- +)$	$Q^{(y)}(L L)$	$Q^{(y)}(R L)$
0	$0.9983 \pm 0.0011$	$-0.01396 \pm 0.00078$	$1.0001 \pm 0.0011$	$-0.0018 \pm 0.0011$	$0.0145 \pm 0.0014$	$0.9906 \pm 0.0014$
0.05	$0.9642 \pm 0.0017$	$0.0195 \pm 0.0015$	$0.9661 \pm 0.0017$	$0.0329 \pm 0.0017$	$0.0480 \pm 0.0019$	$0.9551 \pm 0.0019$
0.1	$0.9300 \pm 0.0021$	$0.0530 \pm 0.0020$	$0.9322 \pm 0.0021$	$0.0674 \pm 0.0021$	$0.0815 \pm 0.0023$	$0.9199 \pm 0.0023$
0.15	$0.8958 \pm 0.0024$	$0.0866 \pm 0.0023$	$0.8983 \pm 0.0024$	$0.1018 \pm 0.0024$	$0.1149 \pm 0.0025$	$0.8849 \pm 0.0026$
0.2	$0.8617 \pm 0.0026$	$0.1201 \pm 0.0026$	$0.8646 \pm 0.0027$	$0.1360 \pm 0.0027$	$0.1482 \pm 0.0028$	$0.8501 \pm 0.0028$
0.25	$0.8275 \pm 0.0028$	$0.1537 \pm 0.0028$	$0.8311 \pm 0.0029$	$0.1700 \pm 0.0029$	$0.1814 \pm 0.0030$	$0.8156 \pm 0.0030$
0.3	$0.7934 \pm 0.0030$	$0.1872 \pm 0.0030$	$0.7976 \pm 0.0031$	$0.2038 \pm 0.0031$	$0.2146 \pm 0.0031$	$0.7813 \pm 0.0032$
0.35	$0.7593 \pm 0.0032$	$0.2208 \pm 0.0032$	$0.7643 \pm 0.0032$	$0.2375 \pm 0.0032$	$0.2477 \pm 0.0033$	$0.7472 \pm 0.0033$
0.4	$0.7252 \pm 0.0033$	$0.2543 \pm 0.0033$	$0.7310 \pm 0.0034$	$0.2709 \pm 0.0034$	$0.2806 \pm 0.0034$	$0.7133 \pm 0.0034$
0.45	$0.6911 \pm 0.0034$	$0.2879 \pm 0.0034$	$0.6979 \pm 0.0035$	$0.3042 \pm 0.0035$	$0.3135 \pm 0.0035$	$0.6796 \pm 0.0035$
0.5	$0.6570 \pm 0.0035$	$0.3215 \pm 0.0035$	$0.6649 \pm 0.0035$	$0.3373 \pm 0.0035$	$0.3464 \pm 0.0036$	$0.6462 \pm 0.0036$
0.55	$0.6230 \pm 0.0035$	$0.3552 \pm 0.0036$	$0.6321 \pm 0.0036$	$0.3702 \pm 0.0036$	$0.3791 \pm 0.0036$	$0.6130 \pm 0.0037$
0.6	$0.5889 \pm 0.0036$	$0.3888 \pm 0.0037$	$0.5993 \pm 0.0037$	$0.4030 \pm 0.0036$	$0.4118 \pm 0.0037$	$0.5799 \pm 0.0037$

TABLE II. Experimental conditional probabilities in the PD channel, from the family of P channels.

$q$	$Q^{(z)}(H H)$	$Q^{(z)}(V H)$	$Q^{(x)}(+ +)$	$Q^{(x)}(- +)$	$Q^{(y)}(L L)$	$Q^{(y)}(R L)$
0	1.0005 ± 0.0015	-0.0163 ± 0.0014	1.0023 ± 0.0015	-0.0040 ± 0.0015	0.0124 ± 0.0017	0.9928 ± 0.0017
0.05	1.0008 ± 0.0015	-0.0162 ± 0.0014	0.9766 ± 0.0019	0.0214 ± 0.0019	0.0375 ± 0.0020	0.9664 ± 0.0020
0.1	1.0012 ± 0.0015	-0.0161 ± 0.0014	0.9509 ± 0.0022	0.0469 ± 0.0022	0.0625 ± 0.0023	0.9402 ± 0.0023
0.15	1.0016 ± 0.0015	-0.0160 ± 0.0014	0.9252 ± 0.0024	0.0723 ± 0.0024	0.0875 ± 0.0025	0.9140 ± 0.0025
0.2	1.0019 ± 0.0015	-0.0159 ± 0.0014	0.8996 ± 0.0026	0.0977 ± 0.0026	0.1124 ± 0.0027	0.8880 ± 0.0027
0.25	1.0023 ± 0.0015	-0.0159 ± 0.0014	0.8740 ± 0.0028	0.1232 ± 0.0028	0.1374 ± 0.0028	0.8620 ± 0.0029
0.3	1.0027 ± 0.0015	-0.0158 ± 0.0014	0.8484 ± 0.0029	0.1485 ± 0.0029	0.1623 ± 0.0030	0.8361 ± 0.0030
0.35	1.0030 ± 0.0015	-0.0157 ± 0.0014	0.8228 ± 0.0030	0.1739 ± 0.0030	0.1871 ± 0.0031	0.8103 ± 0.0031
0.4	1.0034 ± 0.0015	-0.0156 ± 0.0014	0.7973 ± 0.0032	0.1993 ± 0.0032	0.2120 ± 0.0032	0.7846 ± 0.0033
0.45	1.0038 ± 0.0015	-0.0155 ± 0.0014	0.7719 ± 0.0033	0.2246 ± 0.0033	0.2368 ± 0.0033	0.7590 ± 0.0034
0.5	1.0042 ± 0.0015	-0.0154 ± 0.0014	0.7464 ± 0.0034	0.2499 ± 0.0034	0.2616 ± 0.0034	0.7334 ± 0.0034
0.55	1.0045 ± 0.0015	-0.0153 ± 0.0014	0.7210 ± 0.0034	0.2752 ± 0.0034	0.2864 ± 0.0035	0.7080 ± 0.0035
0.6	1.0049 ± 0.0015	-0.0152 ± 0.0014	0.6956 ± 0.0035	0.3005 ± 0.0035	0.3111 ± 0.0035	0.6826 ± 0.0036
0.65	1.0052 ± 0.0015	-0.0151 ± 0.0014	0.6702 ± 0.0036	0.3257 ± 0.0036	0.3359 ± 0.0036	0.6573 ± 0.0036
0.7	1.0056 ± 0.0015	-0.0150 ± 0.0014	0.6449 ± 0.0036	0.3510 ± 0.0036	0.3605 ± 0.0036	0.6321 ± 0.0037
0.75	1.0060 ± 0.0015	-0.0150 ± 0.0014	0.6196 ± 0.0037	0.3762 ± 0.0037	0.3852 ± 0.0037	0.6070 ± 0.0037
0.8	1.0063 ± 0.0015	-0.0149 ± 0.0014	0.5944 ± 0.0037	0.4013 ± 0.0037	0.4098 ± 0.0037	0.5819 ± 0.0037
0.85	1.0067 ± 0.0015	-0.0148 ± 0.0014	0.5691 ± 0.0037	0.4265 ± 0.0037	0.4345 ± 0.0037	0.5570 ± 0.0037
0.9	1.0071 ± 0.0015	-0.0147 ± 0.0014	0.5439 ± 0.0037	0.4517 ± 0.0038	0.4590 ± 0.0037	0.5321 ± 0.0038
0.95	1.0075 ± 0.0014	-0.0146 ± 0.0014	0.5187 ± 0.0037	0.4768 ± 0.0038	0.4836 ± 0.0037	0.5073 ± 0.0038
1	1.0079 ± 0.0014	-0.0145 ± 0.0014	0.4936 ± 0.0037	0.5019 ± 0.0038	0.5081 ± 0.0037	0.4826 ± 0.0038

and  $V_{\text{high}} = 25.0$  V, respectively. We confirmed a visibility of 0.989 between these two voltages, which represents a much higher value than the fidelity of the state itself, meaning that any slight imperfection of  $\mathbb{I}$  and  $\sigma$  operations will weakly affect the data tendency compared to the noise coming from the state generation.

The third source of error is the error propagation that comes from mixing counts coming from different Pauli operations,

suitably weighted. This error is already included in our Monte Carlo simulations.

#### APPENDIX D: EXPERIMENTAL CONDITIONAL PROBABILITIES

In this Appendix, we show the tables of all two-photon conditional probabilities  $Q^{(\alpha)}(A|B)$  extracted from the

TABLE III. Experimental conditional probabilities in the D channel, from the family of P channels.

$q$	$Q^{(z)}(H H)$	$Q^{(z)}(V H)$	$Q^{(x)}(+ +)$	$Q^{(x)}(- +)$	$Q^{(y)}(L L)$	$Q^{(y)}(R L)$
0	0.9983 ± 0.0011	-0.01396 ± 0.00078	1.0001 ± 0.0011	-0.0018 ± 0.0011	0.0145 ± 0.0014	0.9906 ± 0.0014
0.017	0.9642 ± 0.0017	0.0195 ± 0.0015	0.9661 ± 0.0017	0.0329 ± 0.0017	0.0480 ± 0.0019	0.9551 ± 0.0019
0.033	0.9300 ± 0.0021	0.0530 ± 0.0020	0.9322 ± 0.0021	0.0674 ± 0.0021	0.0815 ± 0.0023	0.9199 ± 0.0023
0.05	0.8958 ± 0.0024	0.0866 ± 0.0023	0.8983 ± 0.0024	0.1018 ± 0.0024	0.1149 ± 0.0025	0.8849 ± 0.0026
0.067	0.8617 ± 0.0026	0.1201 ± 0.0026	0.8646 ± 0.0027	0.1360 ± 0.0027	0.1482 ± 0.0028	0.8501 ± 0.0028
0.083	0.8275 ± 0.0028	0.1537 ± 0.0028	0.8311 ± 0.0029	0.1700 ± 0.0029	0.1814 ± 0.0030	0.8156 ± 0.0030
0.1	0.7934 ± 0.0030	0.1872 ± 0.0030	0.7976 ± 0.0031	0.2038 ± 0.0031	0.2146 ± 0.0031	0.7813 ± 0.0032
0.117	0.7593 ± 0.0032	0.2208 ± 0.0032	0.7643 ± 0.0032	0.2375 ± 0.0032	0.2477 ± 0.0033	0.7472 ± 0.0033
0.133	0.7252 ± 0.0033	0.2543 ± 0.0033	0.7310 ± 0.0034	0.2709 ± 0.0034	0.2806 ± 0.0034	0.7133 ± 0.0034
0.15	0.6911 ± 0.0034	0.2879 ± 0.0034	0.6979 ± 0.0035	0.3042 ± 0.0035	0.3135 ± 0.0035	0.6796 ± 0.0035
0.167	0.6570 ± 0.0035	0.3215 ± 0.0035	0.6649 ± 0.0035	0.3373 ± 0.0035	0.3464 ± 0.0036	0.6462 ± 0.0036
0.183	0.6230 ± 0.0035	0.3552 ± 0.0036	0.6321 ± 0.0036	0.3702 ± 0.0036	0.3791 ± 0.0036	0.6130 ± 0.0037
0.2	0.5889 ± 0.0036	0.3888 ± 0.0037	0.5993 ± 0.0037	0.4030 ± 0.0036	0.4118 ± 0.0037	0.5799 ± 0.0037
0.217	0.5549 ± 0.0036	0.4224 ± 0.0037	0.5666 ± 0.0037	0.4356 ± 0.0037	0.4444 ± 0.0037	0.5472 ± 0.0037
0.233	0.5209 ± 0.0036	0.4561 ± 0.0037	0.5341 ± 0.0037	0.4680 ± 0.0037	0.4769 ± 0.0037	0.5145 ± 0.0037
0.25	0.4869 ± 0.0036	0.4898 ± 0.0038	0.5016 ± 0.0037	0.5003 ± 0.0037	0.5093 ± 0.0037	0.4822 ± 0.0037
0.267	0.4529 ± 0.0036	0.5234 ± 0.0038	0.4693 ± 0.0037	0.5324 ± 0.0037	0.5417 ± 0.0037	0.4500 ± 0.0037
0.283	0.4189 ± 0.0036	0.5571 ± 0.0037	0.4371 ± 0.0037	0.5643 ± 0.0037	0.5740 ± 0.0037	0.4180 ± 0.0037
0.3	0.3849 ± 0.0036	0.5908 ± 0.0037	0.4050 ± 0.0036	0.5961 ± 0.0036	0.6062 ± 0.0036	0.3862 ± 0.0036
0.317	0.3509 ± 0.0035	0.6245 ± 0.0037	0.3730 ± 0.0036	0.6276 ± 0.0036	0.6383 ± 0.0036	0.3546 ± 0.0036
0.333	0.3169 ± 0.0034	0.6583 ± 0.0036	0.3411 ± 0.0035	0.6591 ± 0.0035	0.6703 ± 0.0035	0.3232 ± 0.0035

experimental coincidence measurements. We show the results for the AD channel in Table I, the PD channel in Table II, and the D channel in Table III. Due to the

complement rule for orthogonal input states [for instance,  $Q^{(\alpha)}(\cdot|H) = 1 - Q^{(\alpha)}(\cdot|V)$ ], we only show half of the total data.

- 
- [1] I. L. Chuang and M. A. Nielsen, *J. Mod. Opt.* **44**, 2455 (1997).  
 [2] J. F. Poyatos, J. I. Cirac, and P. Zoller, *Phys. Rev. Lett.* **78**, 390 (1997).  
 [3] M. F. Sacchi, *Phys. Rev. A* **63**, 054104 (2001).  
 [4] G. M. D'Ariano and P. Lo Presti, *Phys. Rev. Lett.* **86**, 4195 (2001).  
 [5] G. M. D'Ariano, M. G. A. Paris, and M. F. Sacchi, *Quantum Tomography*, Advances in Imaging and Electron Physics Vol. 128 (Academic Press, San Diego, CA, USA, 2003), pp. 205–308.  
 [6] J. B. Altepeter, D. Branning, E. Jeffrey, T. C. Wei, P. G. Kwiat, R. T. Thew, J. L. O'Brien, M. A. Nielsen, and A. G. White, *Phys. Rev. Lett.* **90**, 193601 (2003).  
 [7] J. L. O'Brien, G. J. Pryde, A. Gilchrist, D. F. V. James, N. K. Langford, T. C. Ralph, and A. G. White, *Phys. Rev. Lett.* **93**, 080502 (2004).  
 [8] M. Riebe, K. Kim, P. Schindler, T. Monz, P. O. Schmidt, T. K. Körber, W. Hänsel, H. Häffner, C. F. Roos, and R. Blatt, *Phys. Rev. Lett.* **97**, 220407 (2006).  
 [9] M. Mohseni, A. T. Rezakhani, and D. A. Lidar, *Phys. Rev. A* **77**, 032322 (2008).  
 [10] I. Bongioanni, L. Sansoni, F. Sciarrino, G. Vallone, and P. Mataloni, *Phys. Rev. A* **82**, 042307 (2010).  
 [11] Y. Sagi, I. Almog, and N. Davidson, *Phys. Rev. Lett.* **105**, 053201 (2010).  
 [12] C. Macchiavello and M. Rossi, *Phys. Rev. A* **88**, 042335 (2013).  
 [13] A. Orioux, L. Sansoni, M. Persechino, P. Mataloni, M. Rossi, and C. Macchiavello, *Phys. Rev. Lett.* **111**, 220501 (2013).  
 [14] D. Chruscinski, C. Macchiavello, and S. Maniscalco, *Phys. Rev. Lett.* **118**, 080404 (2017).  
 [15] C. Macchiavello and M. F. Sacchi, *Phys. Rev. Lett.* **116**, 140501 (2016).  
 [16] C. Macchiavello and M. F. Sacchi, *Phys. Rev. A* **94**, 052333 (2016).  
 [17] Á. Cuevas, M. Proietti, M. A. Ciampini, S. Duranti, P. Mataloni, M. F. Sacchi, and C. Macchiavello, *Phys. Rev. Lett.* **119**, 100502 (2017).  
 [18] V. Cimini, I. Gianani, M. F. Sacchi, C. Macchiavello, and M. Barbieri, *Phys. Rev. A* **102**, 052404 (2020).  
 [19] A. S. Holevo, *Prob. Inf. Transm.* **9**, 177 (1973).  
 [20] B. Schumacher and M. D. Westmoreland, *Phys. Rev. A* **56**, 131 (1997).  
 [21] A. S. Holevo, *IEEE. Trans. Inf. Theory* **44**, 269 (1998).  
 [22] C. Macchiavello and M. F. Sacchi, *Phys. Rev. Lett.* **123**, 090503 (2019).  
 [23] C. Macchiavello, M. F. Sacchi, and T. Sacchi, *Adv. Quantum Tech.* **3**, 202000013 (2020).  
 [24] C. A. Fuchs, *Phys. Rev. Lett.* **79**, 1162 (1997).  
 [25] A. S. Holevo, *Russian Math. Surv.* **53**, 1295 (1999).  
 [26] C. King and M. B. Ruskai, *J. Math. Phys.* **42**, 87 (2001).  
 [27] G. M. D'Ariano, P. Lo Presti, and M. F. Sacchi, *Phys. Lett. A* **272**, 32 (2000).  
 [28] A. G. White, D. F. V. James, P. H. Eberhard, and P. G. Kwiat, *Phys. Rev. Lett.* **83**, 3103 (1999).  
 [29] D. F. V. James, P. G. Kwiat, W. J. Munro, and A. G. White, *Phys. Rev. A* **64**, 052312 (2001).  
 [30] Á. Cuevas, A. De Pasquale, A. Mari, A. Orioux, S. Duranti, M. Massaro, A. Di Carli, E. Roccia, J. Ferraz, F. Sciarrino, P. Mataloni, and V. Giovannetti, *Phys. Rev. A* **96**, 022322 (2017).  
 [31] Y. Yugra, F. De Zela, and Á. Cuevas, *Phys. Rev. A* **101**, 013822 (2020).  
 [32] A. Uhlmann, *J. Phys. A* **34**, 7047 (2001).  
 [33] V. Giovannetti and R. Fazio, *Phys. Rev. A* **71**, 032314 (2005).  
 [34] C. King, *J. Math. Phys.* **43**, 4641 (2002).